WCTE Auckland New Zealand
15 - 19 July 2012
World Conference on Timber Engineering

BRITTLEHEART AS A CRITICAL FEATURE FOR VISUAL STRENGTH GRADING OF TROPICAL HARDWOOD – APPROACH OF DETECTION

Hanna Kuisch[1,2], Wolfgang Gard[1], Erik Botter[2], Jan-Willem van de Kuilen[1,3]

ABSTRACT: Brittleheart is a well-known phenomenon in many tropical wood species which reduces the strength properties considerably. According to national strength grading standards such as BS 5756 and NEN 5493, timber with brittleheart has to be rejected. In many cases, however, brittleheart is not visible on the outer surface and the cross section of sawn timber. This investigation has been focused on qualitative characterisation of compression failures in tropical hardwood in conjunction with non-destructive detection methods. Five grades of compression failures have been characterised by deformation and displacement of wood tissue. Preliminary results show that CT-scanning is a promising technique for detecting the defined grades. However, limitation of detection is due to the resolution of the scanners and contrast ability of imaging. Quantitative studies of brittleheart on mechanical properties are continuing.

KEYWORDS: Compression failures, brittleheart, morphological characteristics, tropical hardwood, CT scanning

1 INTRODUCTION

Timber intended for structural applications must be free of brittleheart. The term 'brittleheart' is mainly used in wood industry and timber trade, and is related to the presence of compression failures in tropical hardwood. Therefore, in this paper the term 'compression failures will be introduced as a synonym for 'brittleheart'. Compression Failures (CF's) are defects in the wood structure. Their size can range from microscopic failure lines to macroscopic failure areas of several millimetres in width which can affect a great part of the stem's cross section. It is important to detect CF's when timber is strength graded and assigned to a strength class. In Europe, the assignment to strength classes is based on EN 14081 and is determined by visual and/or machine strength grading methods. Certain national standards reject the presence of CF's when assigning timber to a strength class, such as NEN 5493 and BS 5756. CF's reduce the timber strength. In addition, timber with CF's often shows brittle failure when loaded in bending and fails without any prior warnings.

On rough sawn surfaces of tropical hardwood CF's sometimes are very difficult if not impossible to detect with the naked eye. In the most unfavourable situation CF's cannot be detected anyway, even after the final processing step.

Non-destructive methods to detect CF's do not exist yet on industrial level. Until now, the only way to detect CF's is by means of visual inspection. However, this manner is limited to detection of clearly visible CF's, in most cases on planed surfaces. A reliable detection method and methodology, for both less visible and not visible CF's to the naked eye, are required in order to fulfil the requirements of the visual strength grading rules.

The purpose of this research is to investigate morphological characteristics of CF's and identify non-destructive detection techniques to be used for different types of CF's. Finally these characteristics will be related to the bending strength properties of selected tropical hardwood containing different types of CF's. This paper presents a part of the on-going investigation. It describes the morphological characteristics of the CF's in tropical hardwood with the aid of non-destructive detection methods based on X-rays. In order to identify the different types of CF's, first the test specimens of different hardwood species are characterised by visual inspection, CT-scanning (3D), and microscopy.

[1] Hanna Kuisch, Email: h.p.kuisch@student.tudelft.nl
Wolfgang Gard, Email: w.f.gard@tudelft.nl
Jan-Willem van de Kuilen, Email: J.W.G.vandeKuilen@tudelft.nl
Delft University of Technology, Fac. of Civil Engineering & Geosciences, Timber Structures & Wood Technology, P.O. Box 5048, 2600 GA Delft, The Netherlands
[2] Hanna Kuisch, Email: hanna.kuisch@tno.nl
Erik Botter, Email: erik.botter@tno.nl
TNO, Department of Building Materials, P.O. Box 49, 2600 AA Delft, The Netherlands
[3] Jan-Willem van de Kuilen, Email: vandekuilen@wzw.tum.de
Technische Universität München, Holzforschung,Winzererstraße, 80797 München, Germany

2 STATE OF THE ART

Research on CF's in wood has been reported for more than seventy years [1-5]. Many studies regarding CF's and their influence on timber strength properties, accompanied by quantitative analysis, have been conducted on softwood, but less so on tropical hardwood. The morphology of CF's has been examined on softwood species by many researchers. Different terms were used to describe CF's [2-3, 5-12, 14]. For hardwood species only a limited number of researches on the morphology of CF's have been conducted [1, 3-4, 13].

Arnold and Steiger [5: p.57] define CF's in conifers as "defects in the wood structure in the form of buckled cell walls of the wood fibres". They state these CF's as "a well-known natural phenomenon" and as "complex three-dimensional geometric structures with more or less fuzzy boundaries which appear in a broad range of intensities" [5: p.58]. Both Arnold and Steiger [5] and the U.S. Department of Agriculture [14] describe the wide range of appearance of these CF's in softwood species, "from minute deformations in the cell wall to wide bands of several millimetres in width, which can affect more than half of the stem's cross section" [5: p.58]. The appearance of CF's affecting the stem's cross section of hardwood species is also mentioned by Hillis et al. [15]. In their investigation on young and mature karri, *Eucalyptus diversicolor*, it was found that CF's can extend to the full length of the merchantable trunk. They also state that these CF's are extensive at different levels of the tree, but in general not concentric. They found that 20% of the mature trees were affected by CF's.

Different types of appearance exist for CF's on timber surfaces as defined by different authors. Ander and Nyholm [11] present a nomenclature of some of the different types of deformations and their characteristics according to different authors. In addition, Hoffmeyer [8] mentions definitions and characteristics for CF's in softwood, which is based on the microscopic examination of Dinwoodie [2]. The terms provided by Hoffmeyer [8] give the most logic sequence for the appearance of CF's. A simplification of the most important definitions linked to their morphology is as follows:

- slip plane a zone of re-orientation of microfibrils;
- microscopic CF's 2 to 5 slip planes in depth covering more than 2 cell walls in width;
- macroscopic CF's more than 5 slip planes in depth and several microscopic CF's are combined. Appears also as a local stability failure and moderately visible to the naked eye;
- gross stability CF's clearly visible CF's to the naked eye.

With regard to visual grading of timber, CF's are usually difficult to detect, particularly on rough sawn timber, as stated by Arnold and Steiger [5]. By planing the surfaces it is possible to detect some CF's by visual inspection, but only the bigger damages can be detected.

Special efforts, such as optimum lighting may be helpful for a better detection of CF's with the naked eye. However, sometimes CF's could only be detected with microscopic investigation because the failures are too fine. Potential techniques like the ultrasound method and the radiation method, Computerized Tomography (CT) using X-rays, were investigated for softwood [16-18]. It appears that the ultrasonic signals and the detection of the small density differences by X-rays were not distinctive enough to recognize the fine CF's [16]. Sonderegger and Niemz [17] concluded that the ability of CT and scanner technology for CF's detection strongly depends on the resolution of the equipment used. They find that CT could easily detect the larger CF's and that higher resolutions are needed to detect the fine CF's. However, from this literature study it seems that CT scanning has not been used for detection of CF's in hardwood.

3 MATERIAL AND METHODS

3.1 MATERIAL

Four tropical hardwood species were selected for this research. The selection was based on the number of samples with CF's available for each timber species, and the market share of the species. The collected timber was provided by five Dutch wood companies who import these species from Africa, Asia and South-America. The collected timber was visually rejected during grading because of the presence of CF's. The four selected tropical hardwood species are presented in Table 1. The results of sapeli and sapupira are reported in this paper, which are representative for the four species used, in the sense that observed CF's in these two species are comparable in size and magnitude to those observed in the remaining two species.

Table 1: *Selected hardwood species used for research (FSC certified)*

Trade name	Scientific name	Continent of origin
Azobé	*Lophira alata* Banks ex Gaertn.f.	Africa
Louro faia	*Roupale montana* Aubl.	South-America
Sapeli	*Entandrophragma cylindricum* Sprague	Africa
Sapupira	*Hymenolobium spp*	South-America

The dimensions of the samples prepared for the CT-scanner Nanotom (further described in section 3.2) were 20 x 20 x 100mm^3. These samples were also used for the morphological characterisation of the CF's. The samples for the other CT-scanner Somatom (see section 3.2) had dimensions of 72 x 122 x 600mm^3 for both sapeli and sapupira. The specimens used for the Somatom were conditioned at a temperature of 20°C and a relative humidity of 65%, whereas the samples for the Nanotom

were kept in the room with a temperature of around 20°C and a relative humidity of approximately 40%.

3.2 METHODS

Visual characterisation

Different experts have characterized visible CF's on board surfaces of softwood species in two ways. One way is by measuring the width of the CF's [5, 19], and the other way is by visually assigning grades to CF's [9]. Since most of the CF's of the four tropical hardwood species appeared as branched failures on the timber surfaces, the method of visually assigning grades to CF's was preferred and applied. The visual assessment of the visible CF's was based on dry planed timber surfaces having moisture contents less than 15%.

Six grades are used for the visual assessment of the CF's. These grades are based on Hoffmeyer's investigation [9] on CF's in Norway spruce. The specimens used for his research were conditioned at a temperature of 20°C and a relative humidity of 65%. The grades formulated by Hoffmeyer for dry timber surfaces are as follows:

- grade 0 is used when there are no CF's visible;
- grade 1 for CF's not visible in dry wood, but barely visible on wet surfaces;
- grade 2 for visible CF's but very difficult to identify;
- grade 3 for visible CF's but difficult to identify;
- grade 4 for clearly visible CF's;
- grade 5 for very distinct CF's, often with fibre separation.

The classification of the CF's grades is illustrated in Figure 1 for Norway spruce.

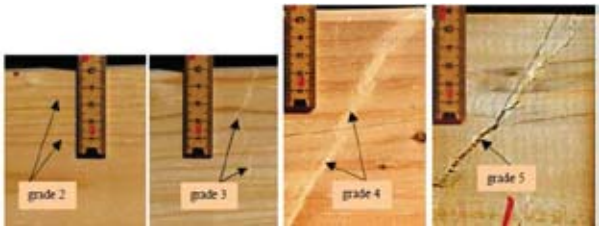

Figure 1: *Classification of CF's grades in softwood [9]*

X-ray scanning

Before scanning the samples with the CT-scanners, samples of each timber species with CF's are visually characterized from grade 0 up to grade 5. The samples for the Nanotom were scanned with a resolution of 30µm x 30µm x 30µm over a length of 30mm, and the samples of the Somatom were scanned with a lower resolution of 0,3mm x 0,3mm x 1,0mm, but over a total length of 200mm. A beam hardening correction of 7,0 was used for the Nanotom samples, and the timing used by the detector to process a single frame was 0,5 seconds. The samples for the Somatom are scanned with the spiral scan mode and with a slice distance of 1,0mm. The scan settings used for both scanners are given in Table 2. These settings determine the contrast of the scan images obtained.

Table 2: *Scan settings used for scanning the samples*

Settings	Nanotom	Somatom
Voltage	90 kV	140 kV
Current	120 µA	250 mA
Filter	-	B50s

Both CT-scanners detect variations in densities represented by different grey values in an image. In our research a low density is represented by a black colour, whereas a high density is represented by a white colour.

Microscopic characterisation

To determine the morphological characteristics of the CF's on the timber, a light microscope and an environmental scanning electron microscope (ESEM) are used. The magnifications used for the light microscope were in the range from 6,3x up to 50x and for the ESEM from 100x up to 2000x. The ESEM is used for the morphological characteristics of the CF's on wood cell level.

4 RESULTS

4.1 MORPHOLOGICAL CHARACTERISTICS

Visual characteristics

Different types of CF grades on a dry and wet surface are illustrated in Figure 2 and 3 (identical samples) for sapeli, and in Figure 4 and 5 for sapupira (identical samples). These figures also show the development of CF's grades within one damaged area. If the surface of the sample is slightly moistened with water (Figure 3), the development and branching of the CF's become more expressed, compared to dry surfaces (Figure 2). As shown in Figure 3 and Figure 5 (at the arrows), even CF's grade 1 become visible. The appearance of the CF's in Figure 2 to Figure 5 are representative for all wood species examined. The development of grades within one damaged zone was an important characteristic for all four species. The occurrence of only one CF grade on the timber surface was hardly noticed.

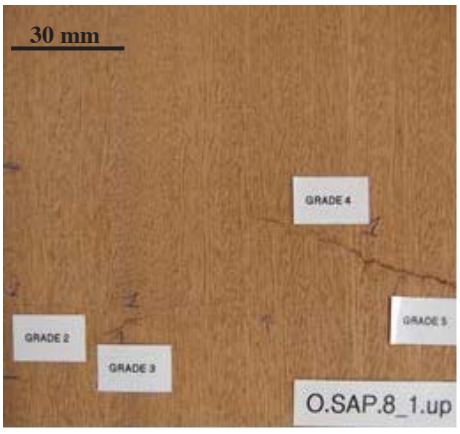

Figure 2: *Classification of CF's grades for a sapeli beam – dry surface*

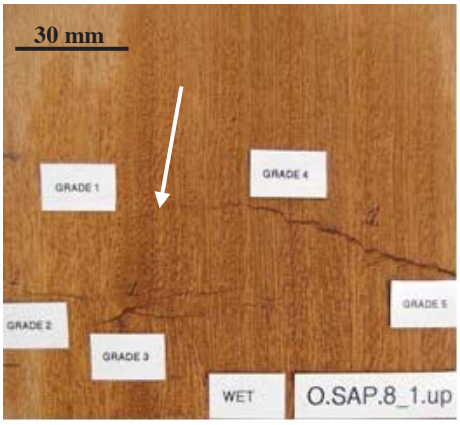

Figure 3: *Classification of CF's grades for a sapeli beam – wet surface displaying grade 1 (see arrow)*

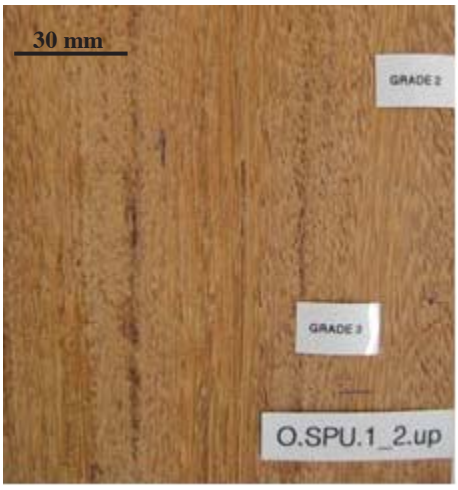

Figure 4: *Classification of CF's grades for a sapupira beam – dry surface*

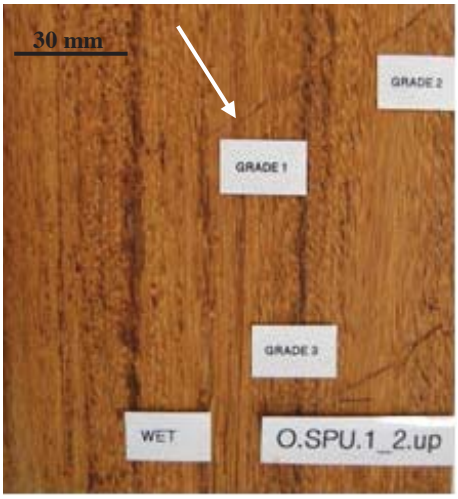

Figure 5: *Classification of CF's grades for a sapupira beam – wet surface displaying grade 1 (see arrow)*

Microscopic characteristics

The CF's are also microscopically investigated. The anatomical structure for different grades on the longitudinal sections is presented in Figure 6 to 9. These pictures are obtained by the light microscope with a magnification of 40x to 50x. Figure 6 shows CF's grade 1 (image A) and grade 4 (image B) on a tangential section of a sapeli sample, and Figure 7 for CF's grade 4 and 5 on a tangential section of a sapupira sample. These figures illustrate localized buckling of the wood cells in the tangential direction for the large CF's (grade 4 in Figure 6 and 7). The buckling shape is either a horizontal displacement or a combination of horizontal and vertical displacements. The morphological structure of the fine CF's (grade 1) are barely visible and showing no distinct fibre buckling (Figure 6A). These fine CF's appear as fine lines on the wood surface. The CF grade 5 is characterised by broken fibres (Figure 7).

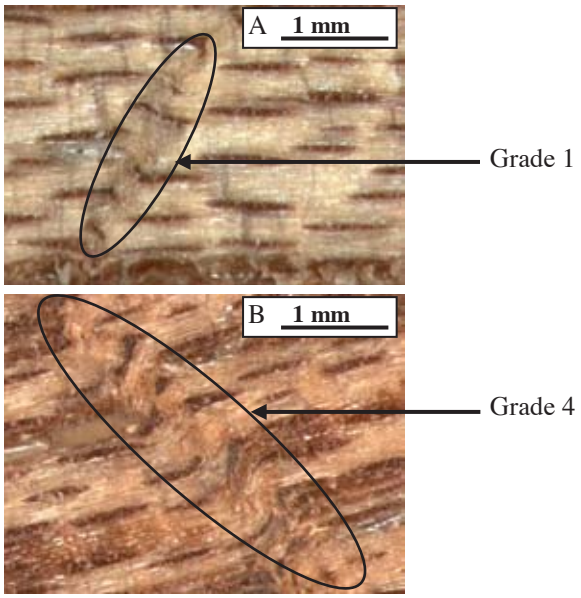

Figure 6: *Sapeli, CF's grades 1 (A) and 4 (B) on a longitudinal tangential plane. Magnification 50x*

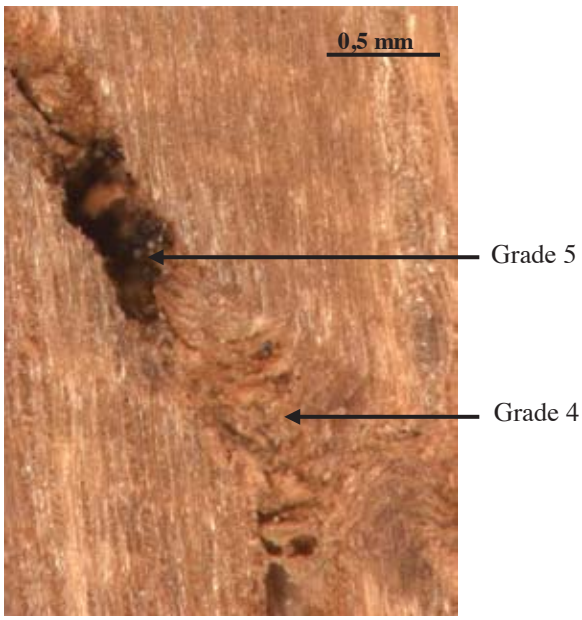

Figure 7: *Sapupira, CF's grades 4 and 5 on a longitudinal tangential plane. Magnification 50x*

The longitudinal radial sections are shown in Figure 8 for a sapeli sample for CF's grade 2 and 4, and in Figure 9 for a sapupira sample for CF's grade 4. Often the CF's on the radial sections appear as straight lines or compressed areas perpendicular to the fibre direction. This orientation of the CF's applies to both the large and fine CF's. Furthermore, the CF's grade 4 on the radial sections (Figure 8 and 9) show no buckling of the fibres compared to the tangential sections (Figure 6 and 7).

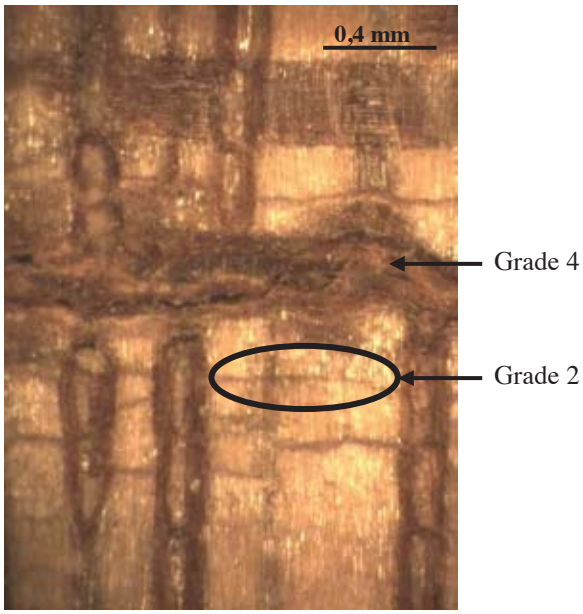

Figure 8: *Sapeli, CF's grades 2 and 4 on a longitudinal radial plane. Magnification 40x*

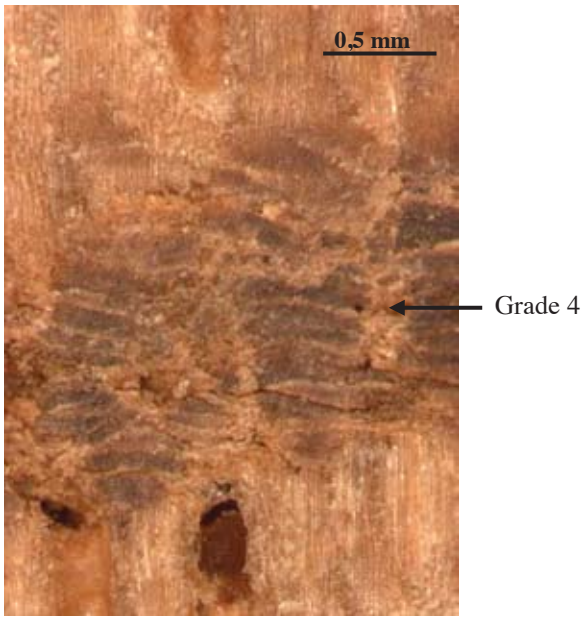

Figure 9: *Sapupira, CF grade 4 on a longitudinal radial plane. Magnification 50x*

The morphological characteristics of the CF's can be observed and analysed to more detail using the ESEM. In Figure 10 large buckling and compression of the wood fibres is clearly visible on the tangential plane section (see arrow). The picture presented applies to CF grade 4 on a sapeli tangential plane.

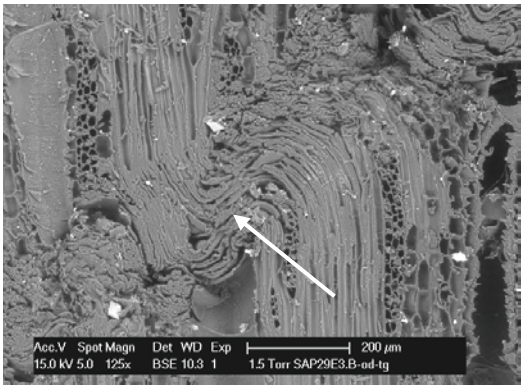

Figure 10: *ESEM, sapeli CF grade 4 with large deformations and displacements of the wood fibres (see arrow). Tangential plane, magnification 125x*

A horizontal displacement of fibre and ray cells can also be observed on the sapupira tangential plane, see arrows in Figure 11. As before, CF grade 5 is characterised by broken fibres, as shown in Figure 12 (see arrows).

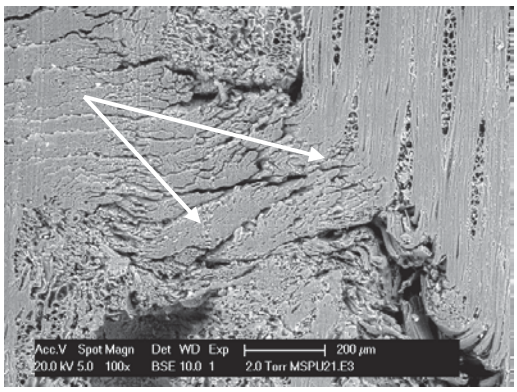

Figure 11: *ESEM, sapupira CF grade 4 showing horizontal displacements of fibre and ray cells (see arrows). Tangential plane, magnification 100x*

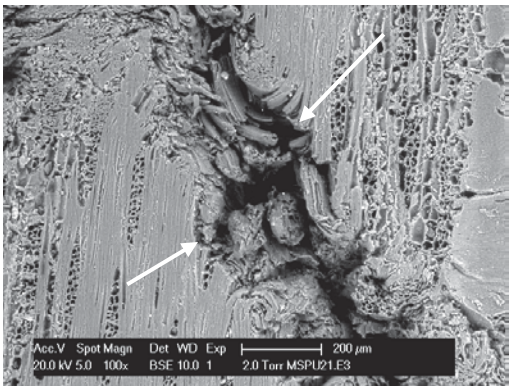

Figure 12: *ESEM, sapupira CF grade 5 with broken wood fibres (see arrows). Tangential plane, magnification 100x*

Figure 13 shows a typical example of CF's grade 1 (see white arrow), and even smaller (see black arrow). Here

also fibre buckling is seen for these failures, but in a less pronounced manner.

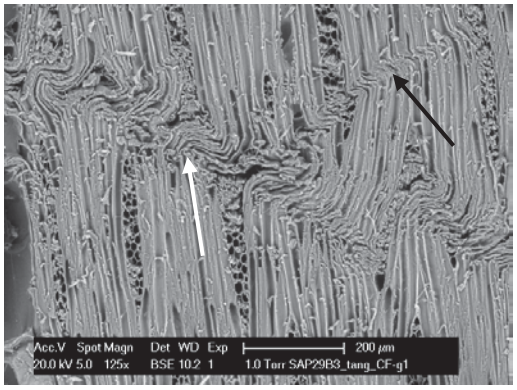

Figure 13: *ESEM, sapeli CF grade 1 (see white arrow) and smaller (see black arrow) showing fibre buckling. Tangential plane, magnification 125x*

Moreover, the compression of wood fibres perpendicular to the horizontal part of the fibre length has deformed the cell cross section (Figure 14). This deformation has been in such a way that the cell lumens are hardly noticeable anymore as illustrated in Figure 14 (see arrows). The figure shows a radial/tangential plane, where the end grain of the deformed wood fibres are visible on the radial part. The cracks visible between the fibres cannot be interpreted as a characteristic of the CF's. These cracks could be caused by the preparation of the sample. The failure zone applies to CF grade 2 on the wood surface.

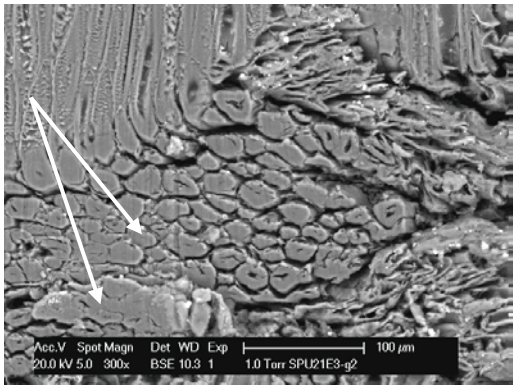

Figure 14: *ESEM, sapupira CF grade 2 showing end grain of the deformed wood fibres (see arrow). Radial/tangential plane, magnification 300x*

4.2 RESULTS OF THE DIFFERENT CT-SCANNING DETECTIONS

In this paragraph first the scan results of the 3D Nanotom are presented, followed by the 3D scan results of the Somatom.

Nanotom

A schematic illustration of the scanned sample with the positions of the displayed planes of Figure 16 is given in Figure 15. This illustration also shows the orientation of the x, y, and z-axis used in Figure 16 for the z-x planes A to D.

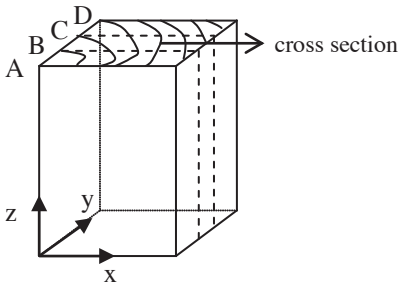

Figure 15: *Schematic illustration of sample with the longitudinal planes A to D*

Figure 16 displays longitudinal images of a Nanotom scan result of a sapupira sample. This sample had visually assigned grades of CF's grade 4 and grade 5 visible at the outer surfaces. The images in Figure 15 present CF's grade 4 on the front outer face (image A), and CF's grade 4 and 5 on the back outer face (image D). The inner faces (image B and C) are obtained by moving in the y-direction (see Figure 15). All these images (A to D in Figure 16) show light-coloured bands of CF's shifting over the cross sectional direction of the sample. In this figure the contrast between the densities of the CF's and the surrounded wood tissue represented by the differences in grey values is visible. Image C shows the development of branching of the CF's. From these pictures it is seen that the appearance of the CF's at the outer surfaces can change over the depth of the sample, and other grades can be present in the inner part of the sample.

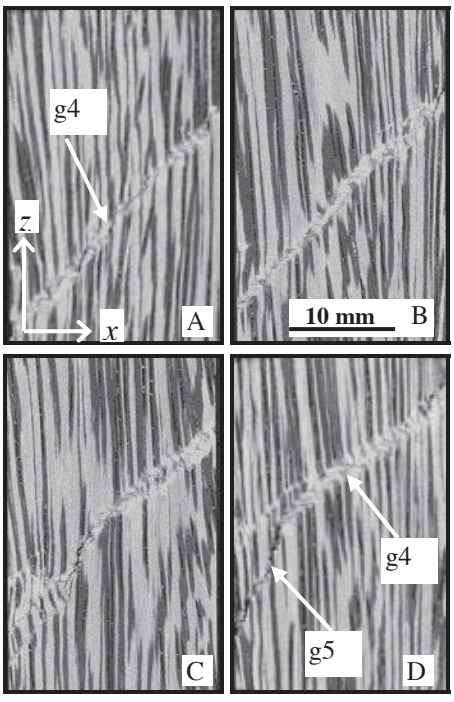

Figure 16: *Light-coloured bands in longitudinal images of a sapupira sample with a grade 4 CF at the outer surface – scanned with the Nanotom*

Figure 17 presents sectional images (A, B, and C) and a 3D image (image D) of a sapupira sample scanned with the Nanotom. The longitudinal section (image B) displays an inner layer about one quarter of the wood cube and the other longitudinal section (image C) displays an inner layer about halfway of the wood cube. Image D presents a 3D view of the wood cube where only the highest densities have been selected. In this view it is noticed that the 'white' bands of the sectional images (see red cross) are represented by these higher densities.
The contrast between the densities of the CF's and the surrounded wood tissue is visible for all CF's grades in the sectional images. This observation counts for all four wood species scanned with the Nanotom.

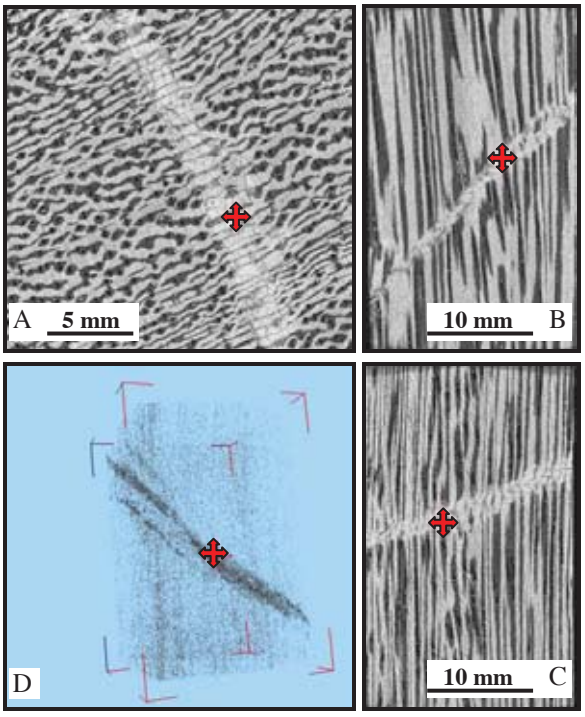

Figure 17: *Sectional images (A, B, and C) and 3D image (D) of a sapupira sample – CF grade 4. Red cross indicates the position in the cube. 3D illustration shows higher densities where 'white' bands are present – scanned with the Nanotom*

Figure 18 shows a longitudinal section of a sapeli sample scanned with the Nanotom. From this picture it is clear that the Nanotom is also able to detect the fine CF's, such as grade 1. The detection of the CF's grade 1 applies to all four hardwood species examined. In some cases even finer lines than defined as CF's grade 1 have been detected.

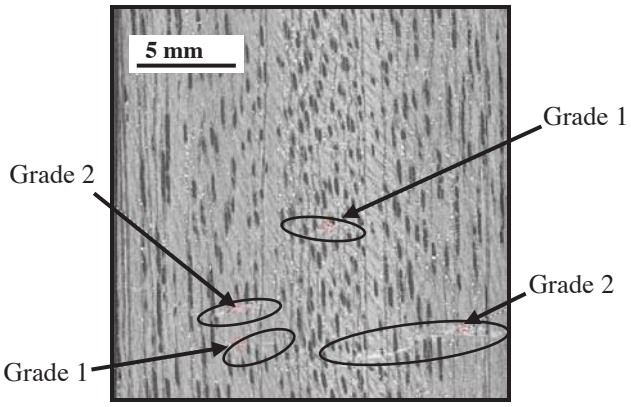

Figure 18: *Longitudinal section of a sapeli sample scanned with the Nanotom – CF's grade 1 and grade 2*

Somatom
Figure 19 presents sectional images (A, B, and C) and a 3D image (image D) of a sapeli beam scanned with the Somatom. The white zones representing the CF's grade 4, show a clear contrast with the surrounding wood tissue. Image D illustrates a 3D view of the beam for only the highest densities. This 3D view shows the geometry of the CF's existing in the beam. The white zones are pointed out by the red cross in the four images (A to D).

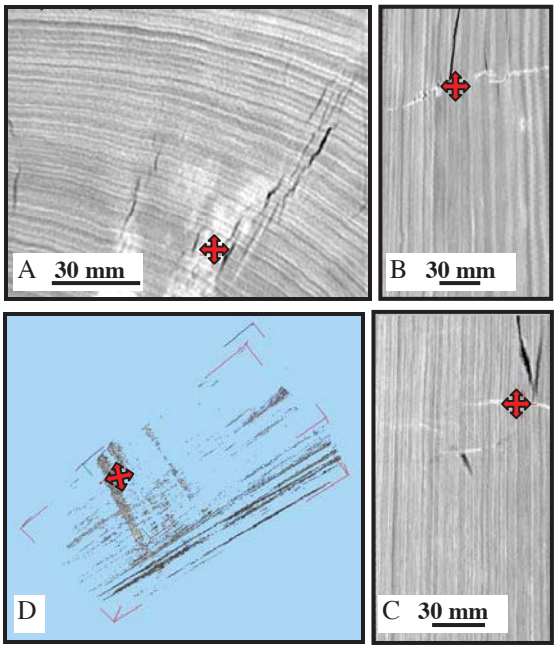

Figure 19: *Sectional and 3D images of a sapeli beam scanned with the Somatom – red cross positioned in white zones represents CF's*

Figure 20 illustrates sectional images (A, B, and C) and a 3D image (image D) of a sapupira beam scanned with the Somatom. The barely visible light grey wrinkles representing the CF's grade 4, show an unclear contrast with the surrounding wood tissue, contrary to the sapeli beam of Figure 19. This is caused by the diffuse density distribution in the sapupira sample.
The wrinkles are pointed out by the red cross in the four images. Image D illustrates a 3D view of the beam for

only the highest densities. However, the expected higher densities for the wrinkles are not visibly represented in the 3D image. This 3D image shows higher densities for other locations in the wood structure.
The sectional images (B and C) also show white zones in the longitudinal direction of the wood structure, representing higher densities than the surrounding wood structure. These white zones are also visible in image A following the orientation of the growth rings. Probably these white zones are represented in image D having the higher densities.

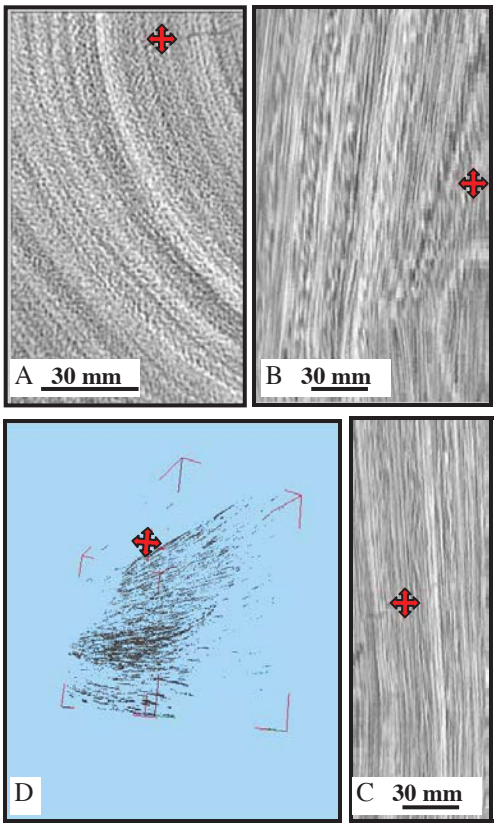

Figure 20: *Sectional and 3D images of a sapupira beam scanned with the Somatom – red cross positioned in the light grey wrinkles represents CF's*

During this investigation it has been noticed that the sapupira samples contain areas with higher distinctive densities, compared with the surrounding tissue. The high density areas were not linked to the CF's zones, but are part of the wood tissue. These higher densities are shown in Figure 21 by the white spots (see red cross) in the four images (A to D). It is noticed that the CF's which are also present in the beam, but having a lower density than the white spots, cannot be displayed in the 3D view (image D).

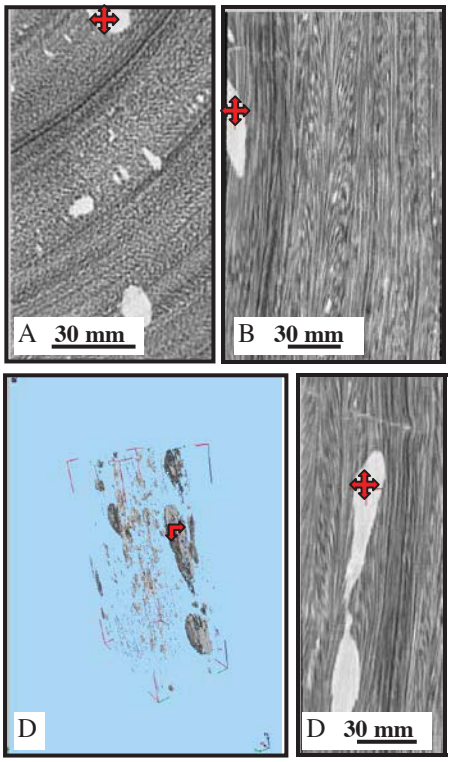

Figure 21: *Sectional and 3D images of a sapupira beam scanned with the Somatom – red cross positioned in the white spots represents resin pockets*

The limit of detection of CF's grades by the Somatom depends on the wood species scanned. For sapeli CF's grades 2 to 5 have been detected (Figure 22, left), whereas for sapupira (Figure 22, right) CF's grade 3 to 5 could be detected.

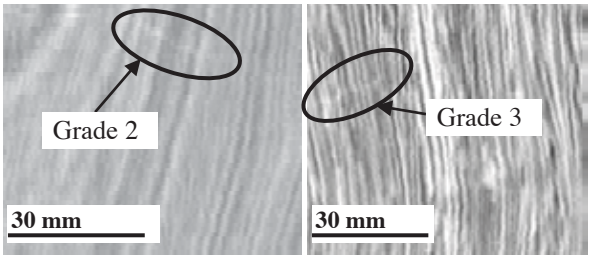

Figure 22: *Longitudinal images. Left: sapeli beam with CF grade 2. Right: sapupira beam with CF grade 3*

5 DISCUSSION

5.1 MORPHOLOGICAL CHARACTERISTICS

Mechanical properties such as bending and tensile strength are about forty times higher in the direction parallel to the fibres, than perpendicular to the fibre direction. Therefore, the orientation of the fibres in the CF's zones influence the strength properties. The orientation and the condition of the fibres have been chosen as a microscopic characteristic for the different CF's grades. In the definition of the CF's by Hoffmeyer [9] these microscopic characteristics have not been reported.

For the visual characteristics all CF's grades appear as fault lines on the surface. These fault lines have an angle between one and ninety degrees parallel to the fibre direction.
On the light microscope a maximum magnification of 50x has been used. On this level different types of appearance for the microscopic characteristics of the CF's grades have been distinguished on the tangential and radial planes. The CF grade 1 still appears as a line on the tangential and radial planes, while the CF's grade 2 to 4 show buckling of the wood cells (Figure 6). These observations apply to the tangential plane. On the radial plane dark lines or areas of highly compressed wood tissue has been observed for the CF's grades 2 to 4. The CF's grade 5 has been characterised as broken fibres on both planes.
The fine failures grade 1 show slightly horizontal displacements of the fibres when higher magnifications has been used, such as 125x obtained by the ESEM (Figure 13). Larger deformations and buckling of the wood tissue has been observed for the CF's grades 2 to 4. The difference between the grades depends on the volume of deformed and displaced fibres, and the obtained strain level of the horizontal displacement. Due to the complexity of fibre orientation and buckling, it is not clear which stress component leads to the rupture of fibres (CF's grade 5). It is possible that the increased longitudinal compressive stresses lead to tensile stress components on the changed fibre direction, or to tensile stresses perpendicular to the original fibre axis.

5.2 CT-SCANNING DETECTIONS

3D CT-scanning should have two advantages. Firstly, to be able to follow the propagation of the CF's in the beam. Secondly, to be able to use this technique for the non-destructive detection of CF's on an industrial level.
The most interesting finding is the limit of detection of the Nanotom, which was able to detect all CF's grades, whereas the Somatom was sensitive to detect some CF's grades depending on the wood species. The differences of capability of CF's detection of both Nanotom and Somatom are caused by the voxel resolution and the contrast of the scan images. The contrast can also be influenced by the diffuse density distribution (see Figure 20) within the specimen. The reason for this distribution can be caused by the distribution of high density extractives, such as resins (Figure 21) or crystals.

It is also interesting to note that the Nanotom and Somatom display the CF's zones by higher density areas. The higher density is caused by the compression of the fibre and ray cells resulting in squeezed cell wall material. This is confirmed by the ESEM pictures (Figure 14). The higher density for CF's counts for CF's having a visually assigned grade up to grade 4. Since a crack is detected as open space by the CT-scanners, a low density is assigned to this area represented by black zones. Thus, CF's grade 5 characterized by fibre rupture should have a lower density than the surrounding wood tissue.

Besides the limits of detection for CF's grades, also detection limits exist with regard to the sizes of the samples. For the examination on the Nanotom, the sample sizes are restricted to 100 x 100 x 290 mm^3, and the Somatom can scan cross sections up to 300 x 400 mm^2. Regarding the length of the samples for the Somatom, no length limitation exists. With this CT-scanner however, the scan length is limited to 2000 mm.

6 CONCLUSIONS

The purpose of this paper is to present the qualitative characterisation and non-destructive detection of CF's in tropical hardwood. The visual and microscopic characteristics show two classes which can be distinguished. Firstly class 1, where buckling of the wood cells has been observed. This class contains CF's grade 1 (very fine CF, only visible to the naked eye on planed wet wood surfaces) up to grade 4 (clearly visible CF to the naked eye). The difference between the grades depends on the volume of deformed and displaced fibres, and the obtained strain level of the horizontal displacement. Secondly class 2, where class 1 is extended by fibre rupture. This class contains CF's grade 5 (clearly visible CF, accompanied by wood fibre rupture). The different grades were visually assigned to the observed CF's on the timber surfaces. It can be concluded that areas with CF's have a higher density compared with the surrounding wood tissue. CF's grade 5 can also have low density zones where fibres have been separated.

Furthermore, it is concluded that the CT-scanners can detect CF's successfully. The Nanotom (high resolution micro CT-scanner) can detect all CF's grades. The Somatom (medical CT-scanner) can detect CF's starting at grade 2 for sapeli and grade 3 for sapupira. Both types of 3D CT-scanner were able to detect the propagation of different CF's grades throughout the specimens. Hereby the branched CF's and the changeover of divers CF's grades inside the wood could be detected, which could not be linked to the visual grades on the surface of the wood. In this respect 3D CT-scans are able to detect the internal expansion of the CF's.
Besides the limits of detection for CF's grades, also detection limits exist with regard to the cross sectional dimensions of the samples. For the examination on the Nanotom, the sample sizes are restricted to 100 x 100 mm^2, and the Somatom can scan cross sections up to 300 x 400 mm^2.

Recommendations
Further research is needed to quantify the characteristics of the different CF's grades. Special attention should be paid to the volume of the compressed damaged areas, and the extension of the buckling of the wood tissue.
For the non-destructive detection, the 3D CT-scanning technique is a promising method to detect brittleheart in tropical hardwood on an industrial level.

ACKNOWLEDGEMENT

The colleagues from Delft University of Technology, both at the Department of Timber Structures & Wood Technology, Microlab, and at the Department of Geotechnology, are tanked for their contribution to this research. Special thanks to W. Verwaal, P.M. Meijvogel-de Koning, and A. Thijssen for their technical support. Also the colleagues at TNO, Department of Building materials, are thanked for their contribution to this research. The contribution of the Dutch Wood companies who delivered the wood samples for this research is gratefully acknowledged.

REFERENCES

[1] Dadswell, H. E., Langlands, I.: Brittle heart and its relation to compression failures. Emp. For. J. 17:58-65, 1938.
[2] Dinwoodie, J. M.: Failure in timber. Part 1. Microscopic changes in cell-wall structure associated with compression failure. J. Inst. Wood Sci. 21:37-53, 1968.
[3] Kučera, L.J., Bariska, M.: On the fracture morphology in wood. Part 1. A SEM-study of deformations in wood od spruce and aspen upon ultimate axial compression load. Wood Sci. Technol. 16:241-259, 1982.
[4] Yang, J.L.: Bending strength properties of regrowth eucalypt brittleheart. Short Note. Holzforschung 55:183-184, 2001.
[5] Arnold, M., Steiger, R.: The influence of wind-induced compression failures on the mechanical properties of spruce structural timber. Materials and Structures 40:57-68, 2006.
[6] Dinwoodie, J. M.: Failure in timber. Part 3. The effect of longitudinal compression on some mechanical properties. Wood Sci Technol. 12:271-285, 1978.
[7] Wilkins, A.P.: The nomenclature of cell wall deformations. Wood Sci Technol. 20:97-109, 1968.
[8] Hoffmeyer, P.: Failure of wood as influenced by moisture and duration of load. PhD Thesis. State University of New York, 1990.
[9] Hoffmeyer, P.: Mechanical properties of timber from wind damaged Norway spruce. In: L. Salmén (Ed) Proceedings of the second international conference of the European Society for Wood Mechanics, Stockholm, Sweden, 25-28, May 2003.
[10] Malan, F.S.: Eucalyptus improvement for lumber production. Seminário internacional de utilização da Madeira de eucalipto para serraria, São Paulo, Brazil, 1995.
[11] Ander, P., Nyholm, K.: Deformations in wood and spruce pulp fibres: Their importance for wood and pulp properties. In: Proceedings of the international symposium on wood machining, 3-19, 2000.
[12] Horácek, P.: Introduction to tree statics & static assessment. Tree statics and dynamics seminar, interpreting the significance of factors affecting tree structure & health, Westonbirt, UK, 2003.
[13] Scurfield, G., Silva, S.R., Wold, M.B.: Failure of wood under load applied parallel to grain: A study using scanning electron microscopy. Micron 3:160-184, 1972.
[14] U.S. Department of Agriculture: Detection of compression failures in wood. Number 1588. Forest Products Laboratory, Madison, Wisconsin, 1961.
[15] Hillis, W.E., Hardie, A.D.K., Ilic, Y.: The occurrence of brittle heart in Eucalyptus grandis grown in Zambia. In: Proceedings of IUFRO Division 5 meeting, South Africa, 2:485-493, 1973.
[16] Wallace, G.: Defect core detection in radiata pine logs. Report 93/46. Institute of Geological & Nuclear Sciences Limited Lower Hutt, New Zealand, 1993.
[17] Sonderegger, W.; Niemz, P.: The influence of compression failure on the bending, impact bending and tensile strength of spruce wood and the evaluation of non-destructive methods for early detection. Holz Roh Werkst. 62:335-342, 2004.
[18] Brancheriau, L., Lanvin, J-D.: Research into non-destructive compression crack detection methods for wood structures. DGAC study nº 06/084/MQ/FIN, Final report revised version, 2008.
[19] Behzad, K.: Effects of compression failure on the mechanical properties of Pinus wood in an experimental planting in north of Iran. In: ICOMOS IWC – XVI international symposium, Florence, Venice and Vicenza, 2007.

WCTE Auckland New Zealand
15 - 19 July 2012
World Conference on Timber Engineering

BONDED-IN GFRP RODS FOR THE REPAIR OF GLUED LAMINATED TIMBER

Gary Raftery[1], Conor Whelan[2], Annette Harte[3]

ABSTRACT: This paper describes an experimental test programme whereby the use of adhesively bonded-in glass fibre reinforced polymer (GFRP) rods were examined for the reinforcement and repair of artificially fractured glued laminated timber beams. The reinforcement technology was initially tested on control undamaged beams whereby it was seen that the geometrical arrangement of the groove influenced the mechanical performance of the beams. The mechanical behaviour of artificially fractured and fracture repaired beams was subsequently examined. By using practical percentages of reinforcement, strategically located at the soffit of fractured beams, it was seen that the stiffness of the beams can be satisfactorily restored to its original state. Furthermore, a significant increase in ultimate moment capacity can be achieved with the use of these materials. No premature bond failures were recorded while undertaking the testing. The paper also discusses the development of a 3-dimensional finite element model which incorporates anisotropic plasticity theory. The results from the model agree with the experimental testing by demonstrating the performance of the composite system can be enhanced by improving the geometry of the routed out grooves in which the reinforcement is placed. The model also predicted with good accuracy the stiffness of the beams as well as the nonlinear behaviour of the reinforced beams and is a useful tool for further optimisation of the repair system.

KEYWORDS: Glued laminated timber, Repair, Glass fibre reinforced polymers, Finite element modelling

1 INTRODUCTION

Timber is one of the oldest construction materials. As the service requirements that are imposed on structural members change with building function, mechanical repair or upgrade of aging members becomes an important issue. Current procedures for the repair of timber structures vary depending on the level of deterioration of the wood and the required increase in load capacity. Designers in the construction industry are becoming increasingly aware of the advantages offered by fibre reinforced polymer materials for structural repair applications. Technical information on the use of these materials in the rehabilitation of structural members is available in the literature [1]. Guidance is also available in relation to the surveying for repair and rehabilitation work on timber structures [2, 3]. The use of bonded-in reinforcements for upgrading structural timber elements is associated with improved fire protection as well as being visually more attractive in comparison to externally applied reinforcements. Furthermore, mechanical protection is provided to the reinforcement material and the possibility of premature delamination is significantly reduced because of the greater bond area associated with using bonded-in reinforcement techniques.

1.1 OBJECTIVES

This paper describes research undertaken at NUI Galway to examine the use of adhesively bonded-in pultruded glass fibre reinforced polymer (GFRP) rods for the flexural reinforcement and repair of glued laminated timber beams. The paper discusses the results of an extensive experimental test programme whereby the mechanical performance during static loading of unreinforced, reinforced beams using different groove arrangements, artificially fractured and fracture repaired beams are compared. The development of a nonlinear 3-dimensional finite element model, which can accurately predict the mechanical performance of the reinforced beams, is also undertaken. This model can be used to analyse the geometric arrangement of the routed out grooves and also to optimise the repair system.

[1] Gary Raftery, Department of Civil and Environmental Engineering, The University of Auckland, Private Bag 92019, Auckland 1142, New Zealand.
Email: g.raftery@auckland.ac.nz
[2] Conor Whelan, Civil Engineering, College of Engineering and Informatics, National University of Ireland, University Road, Galway, Galway, Ireland.
Email: c.whelan1@nuigalway.ie
[3] Annette Harte, Civil Engineering, College of Engineering and Informatics, National University of Ireland, Galway, University Road, Galway, Ireland.
Email: annette.harte@nuigalway.ie

2 EXPERIMENTAL TESTING

2.1 TEST PROGRAMME

The beam test programme involved the manufacture and testing of twenty five glued laminated timber beams. The five beam types, which were examined, included unreinforced beams, reinforced beams using square shaped grooves, reinforced beams using circular grooves, artificially fractured beams and fracture repaired beams. Five replicates for each beam type were manufactured using mechanically stress graded spruce laminations. An unbiased manufacturing approach was adopted for the lay-up arrangements of the glulam beams whereby the test programme involved careful staggering the laminations in the different beam types based on the mechanical stress grading data. Each of the beams comprised five laminations giving an overall depth of 190 mm and had a span of 3420 mm. The artificially fractured beams had a 3 mm saw kerf through the entire thickness of the bottom lamination at midspan. The reinforced and fracture repaired beams had two 12 mm GFRP rods bonded into routed out grooves that were strategically located in the soffit of the members (Figure 1). A two-part gap filling epoxy adhesive was used for bonding the GFRP rods in both the reinforced and fracture repaired beams. Careful surface preparation of the wood involved vacuum cleaning prior to adhesive bonding and wiping the FRP rods clean with methylated spirits. The fracture repaired beams involved placing the reinforcement into circular shaped grooves only due to the performance difference achieved between the beams reinforced using square shaped grooves and circular shaped grooves. The beam test programme is summarised in Table 1.

2.2 BEAM TESTING

The global and local stiffness of all the glulam beams was initially determined by testing in four point bending as shown in Figure 2. Testing was carried out at the facilities in Civil Engineering at the National University of Ireland, Galway. A linear variable differential transformer (LVDT), which was positioned in a hanger and suspended from the neutral axis over a distance of five times the depth of the beam, was used to measure the local stiffness. These readings were taken in the zone of maximum bending moment. A second LVDT which was inverted on the compression face of the beam, was used to measure the global stiffness of the beam. The global deflection corresponded to the deflection at midspan relative to the supports. The stiffness testing was carried out at a constant crosshead displacement rate of 0.57mm/sec [4]. The beams were laterally supported approximately 300mm outside of the loading heads and polytetrafluoroethylene (PTFE) strips were used to reduce the effects of friction to a minimum. The test configuration shown in Figure 2, was also used for testing the reinforced, artificially fractured and fracture repaired beams. After removal of the local stiffness LVDT and associated hanger, the beams were tested to failure and all beams failed in a time of 300±120 seconds as required by EN408 [4].

Table 1: *Beam test programme*

Beam Types	Repetitions	Beam Numbers
Unreinforced	5	1, 8, 15, 22, 29
Reinforced using square grooves	5	3, 10, 17, 24, 31
Reinforced using circular grooves	5	4, 11, 18, 25, 32
Artificially fractured	5	6, 13, 20, 27, 34
Fracture repaired	5	7, 14, 21, 28, 35

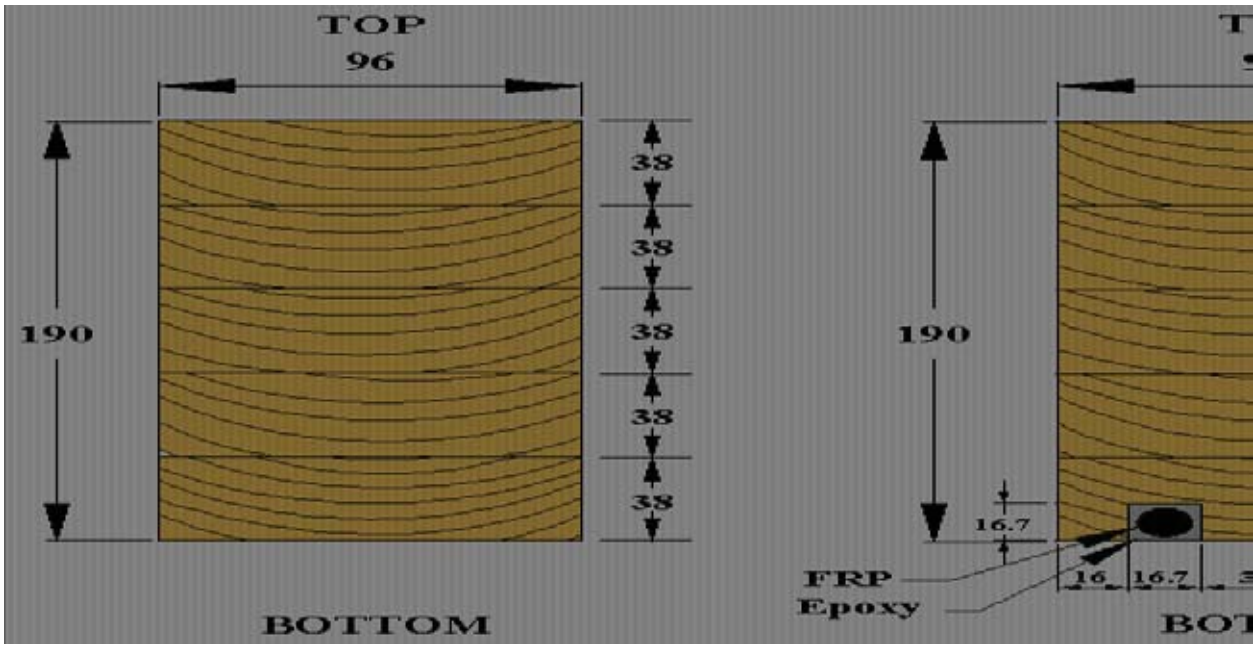

Figure 1: *Arrangements for unreinforced beam, reinforced beam using square grooves and reinforced beam using circular grooves.*

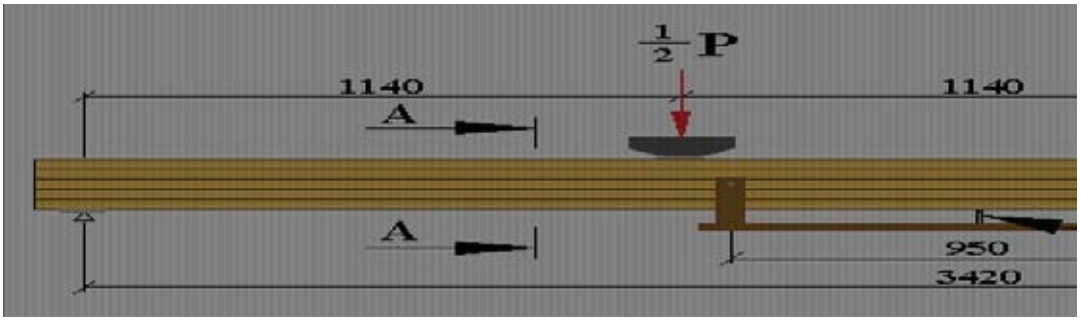

Figure 2: Beam testing arrangement

3 NUMERICAL MODELLING

3.1 MODEL DEVELOPMENT

A 3-dimensional finite element model incorporating anisotropic plasticity has been developed to predict the behaviour of the unreinforced and reinforced beams. The model employs double symmetry and uses 10-noded second order tetrahedral elements. The geometry of the model and loading arrangements corresponded with thetest procedures undertaken during the experimentally testing (Figure 3). Each lamination was modelled as a separate entity so that the material characteristics of the individual laminations could be incorporated in the model. Perfect connections were assumed to exist at the adhesively bonded surfaces between both the wood-wood interfaces and FRP-timber interfaces as no bondline failures in the glulam beams were observed during testing. Furthermore, it has been reported that the epoxy adhesive that was used at the FRP-wood bond interface has formed strong durable bonds in previous test programmes undertaken [5]. The model also includes steel plates at the loading points in order to avoid stress concentrations at these locations.

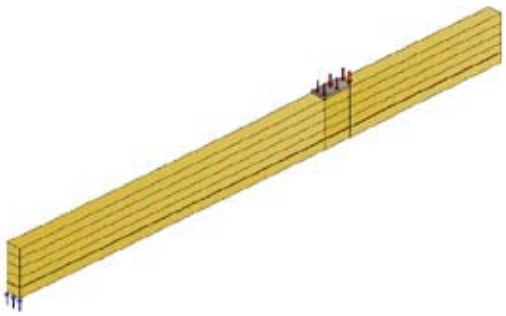

Figure 3: *3-dimensional model with quarter beam modelled*

The end support of the beam was modelled as a roller support by restraining the beam from movement in the vertical direction. Translation of the beam in the longitudinal direction is permitted as was permitted during the experimental testing. The models were loaded by placing a surface pressure load on the steel plates, which in turn transferred the load to the glulam beam. The composite rod reinforcement and surrounding epoxy

are finely meshed with an element edge length of 3 mm in the reinforced beams which included both the square and circular grooves. This is because the stress distribution between the rods, epoxy and timber is of particular interest. The remaining timber laminates and the steel plates are meshed with a larger element edge length of 20 mm. Sections of the fourth and fifth laminations are meshed with elements having non-linear anisotropic material properties. These sections between the loading heads make up the zone of maximum compression at the top of the beam. The loading sequence consisted of separate load steps, each, placing an increasing pressure on the plates which replicated the testing procedure. A static small displacement analysis was executed during each load step and the deflection at midspan and reaction at one of the supports were recorded.

3.2 MATERIAL CHARACTERISATION

The material properties, which were used in the finite element model, were determined from known relationships, published data and secondary test programmes. A linear elastic, perfectly plastic material model was employed for the behaviour of the timber parallel to grain in compression while a linear elastic material model is employed for timber in tension (Figure 4).

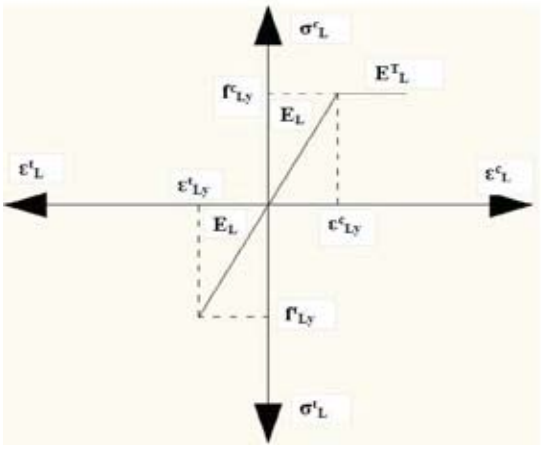

Figure 4: *Stress strain behaviour of timber parallel to grain.*

The finite difference method was used to determine a global modulus of elasticity for each lamination after local readings at 100 mm intervals were determined from the mechanical stress grading procedure.

Anisotropic plasticity theory was employed in the model to include the plastic behaviour of the timber in the top two laminations in the compression zone. The theory includes bi-linear behaviour for the timber in the three orthogonal directions as well as the three shear planes. Therefore, normal compressive yield stresses are declared for the longitudinal, f_{Ly}^{c}, radial, f_{Ry}^{c} and tangential, f_{Ty}^{c} directions as well as yield shear stresses in the three planes. Tangent moduli, E^{T} or tangent shear moduli, G^{T} define the behaviour of the material after yielding. The longitudinal yield stress in compression, f_{Ly}^{c} , was determined from a secondary test programme [6]. A combination of established relationships and published data were used to determine the remaining parameters. While considerable variation is associated with the mechanical properties in wood, the relationship between the Young's moduli in the three timber orientations expressed by Bodig and Jayne [7] in Equation 1 and the relationship between the three shear moduli as expressed in Equation 2 were applied to the timber in the model.

$$E_L:E_R:E_T \approx 20:1.6:1 \quad (1)$$

$$G_{LR}:G_{LT}:G_{RT} \approx 10:9.4:1 \quad (2)$$

where, E_L,E_R,E_T are the Young's moduli in the longitudinal, radial and tangential directions and G_{LR},G_{LT},G_{RT} are the shear moduli in the respective planes. The relationship between $E_L$and G_{LR} as expressed in Equation 3 [7] was also used.

$$E_L:G_{LR} \approx 14:1 \quad (3)$$

Poisson's ratio values of 0.37, 0.47 and 0.43 for ν_{LR}, ν_{LT} and ν_{RT}, respectively, were employed in the finite element model and are given in the literature for Sitka spruce [8]. The tangent moduli E^{T} and the yield stresses f_y, in the three orthogonal directions and shear planes that are used in the model are also available in the literature [9]. The characterisation of the other materials in the model was simpler than modelling the behaviour of the timber. The FRP rod is modelled as a linear elastic orthotropic material with a Young's modulus of 40.8GPa, and the epoxy adhesive and steel are treated as linear elastic isotropic materials.

4 RESULTS

4.1 EXPERIMENTAL TESTING

4.1.1 Load-deflection behaviour

The load-deflection behaviour until failure for the unreinforced series of beams is shown in Figure 5.

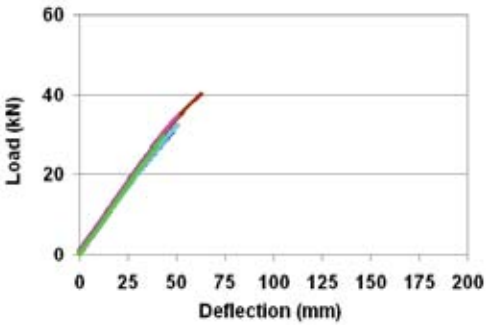

Figure 5: *Load-deflection behaviour of unreinforced beams*

The beams all exhibited linear elastic behaviour until their point of failure. The beams failed through tensile failure of the bottom lamination with the majority of failure cracks emanating from defects in the wood. As can be seen in Figure 6, non-linear behaviour is associated with the reinforced beams with square grooves before failure occurs. Compression buckling was present in all five of the reinforced beams. All beams failed through tension failure of the bottom laminate.

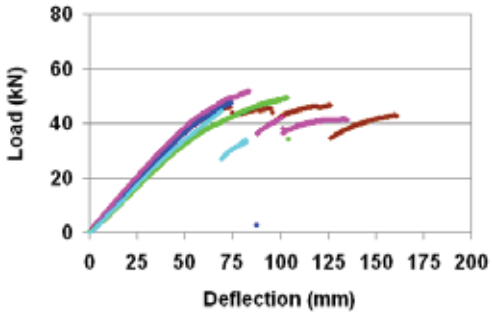

Figure 6: *Load-deflection behaviour of reinforced beams (square grooves).*

In comparison with the reinforced beams which used square grooves, the reinforced beams which used circular grooves experience a significant improvement in the load carrying capacity as seen in Figure 7. It was envisaged prior to testing that the circular routing would create a more favourable stress distribution between the timber and the reinforcement in comparison to the use of square grooves. Judging by the load deflection data the reduction in stress concentrations appears to lead to an increase in load carrying capacity of the beams. All of the beams failed through tensile failure at a defect in the bottom lamination and exhibited large deflections before failure. In a number of the beams, after the timber in the bottom tension lamination failed, the reinforcement took the reduced load. After a period of increasing load and associated large deflection the beams eventually failed through pull out failure of the reinforcement.

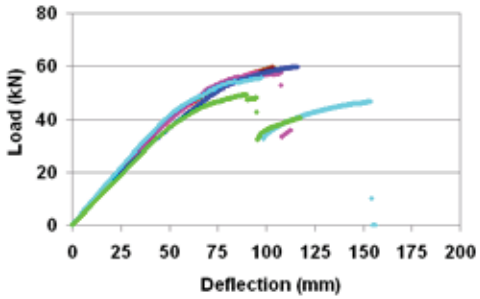

Figure 7: *Load-deflection behaviour of reinforced beams (circular grooves).*

The load-deflection response of the artificially-fractured beams is shown in Figure 8. All five beams failed through tension cracks emanating from the saw kerf. The beams demonstrated linear elastic behaviour before failure and also exhibited lower stiffness as a result of the saw kerf through the bottom tension lamination.

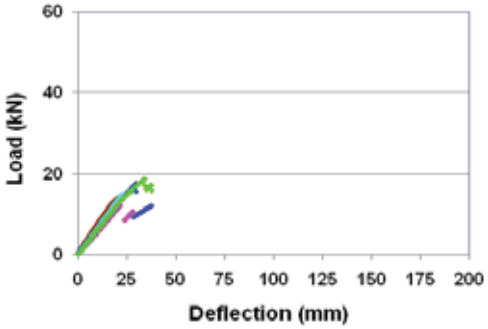

Figure 8: *Load-deflection behaviour of fractured beams*

Figure 9 illustrates the load-deflection behaviour of the fracture repaired beams. All of the beams demonstrated non-linear ductile behaviour before failure. The mechanical performance of the beams is considerably improved when compared to the artificially fractured beams. In addition to this, in comparison with the unreinforced control beams, the beams which included the reinforcement have not only regained their initial load carrying capacity but exceeded this. With FRP material being lightweight and the simple procedure for the near surface mounted technique, these findings highlight their potential for use as a retrofitting and strengthening option.

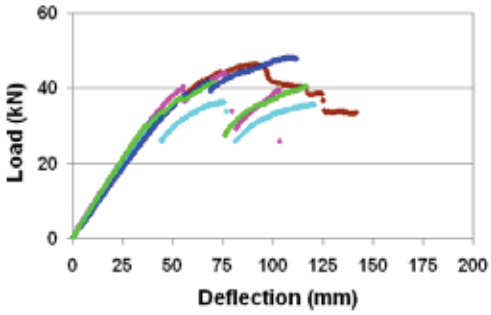

Figure 9: *Load-deflection behaviour of repaired beams*

4.1.2 Stiffness

The stiffness results for the unreinforced glulam beams for both global and local testing are shown in Figure 10. The local bending stiffness (EI) is in the range of 4.7-5 $x10^{11}$ Nmm^2 and the global bending stiffness is in the range 4.9-5.5 $x10^{11}$ Nmm^2. The average local stiffness is 5.164 $x10^{11}$ Nmm^2 and the average global stiffness is 4.852 $x10^{11}$ Nmm^2.

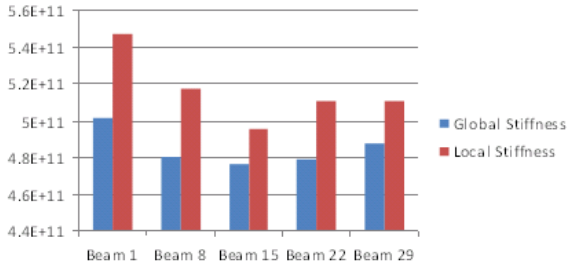

***Figure 10:** Stiffness data for unreinforced beams (Nmm^2).*

The reinforced beams which used square grooves were tested twice in stiffness; after glulam beam fabrication and again after the addition of the 12.7mm diameter GFRP rods. In their unreinforced state, the beams had a mean global stiffness of $4.88x10^{11}$ Nmm^2 with a standard deviation of $0.402x10^{11}$ Nmm^2 and a mean local stiffness of $5.24x10^{11}$ Nmm^2 with a standard deviation of $0.284x10^{11}$ Nmm^2. In their reinforced state, the beams had a mean global stiffness of $5.73x10^{11}$ Nmm^2 with a standard deviation of $0.428x10^{11}$ Nmm^2 and a mean local stiffness of $5.89x10^{11}$ Nmm^2 with a standard deviation of $0.452x10^{11}$ Nmm^2. This corresponds to a mean global stiffness increase of 17.00%, with a 2.08% standard deviation, and a mean local stiffness increase of 12.40% with a 3.60% standard deviation. The results for local stiffness and global stiffness are illustrated in Figure 11 and Figure 12, respectively.

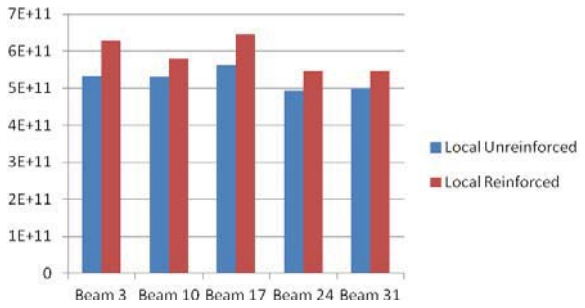

***Figure 11:** Local stiffness data for reinforced (square grooved) beams (Nmm^2).*

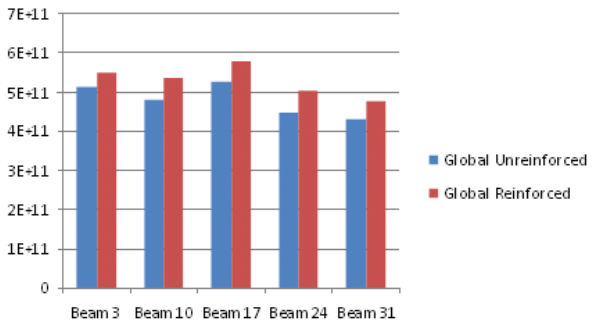

***Figure 12:** Global stiffness data for reinforced (square grooved) beams (Nmm^2).*

The stiffness of the beams, which included reinforcement placed into circular grooves beams, were also tested twice, once in their unreinforced state and then again in their reinforced state. The results in relation to local stiffness and global stiffness are illustrated in Figure 13 and Figure 14, respectively. In their unreinforced state, the beams had a mean global stiffness of $4.88x10^{11}$ Nmm^2 with a standard deviation of $0.402x10^{11}$ Nmm^2 and a mean local stiffness of $5.35x10^{11}$ Nmm^2 with a standard deviation of $0.753x10^{11}$ Nmm^2. In their reinforced state, the beams had a mean global stiffness of $5.73x10^{11}$ Nmm^2 with a standard deviation of $0.428x10^{11}$ Nmm^2 and a mean local stiffness of $6.83x10^{11}$ Nmm^2 with a standard deviation of $0.591x10^{11}$ Nmm^2. After reinforcement was added, the mean global stiffness increased by 17.47%, with a 2.09% standard deviation, and the mean local stiffness increased by 27.48% with a 9.00% standard deviation. This shows a marked increase in stiffness with the addition of the reinforcement in circular grooves in comparison with the reinforcement being placed in square grooves.

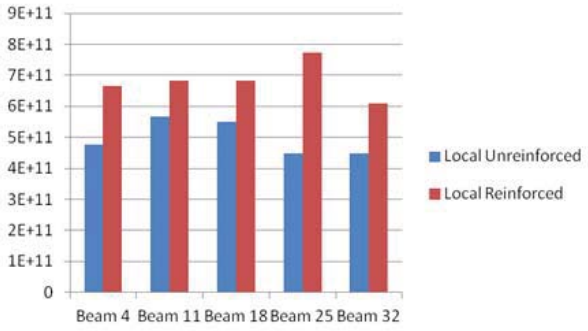

***Figure 13:** Local stiffness data for reinforced (circular grooved) beams (Nmm^2).*

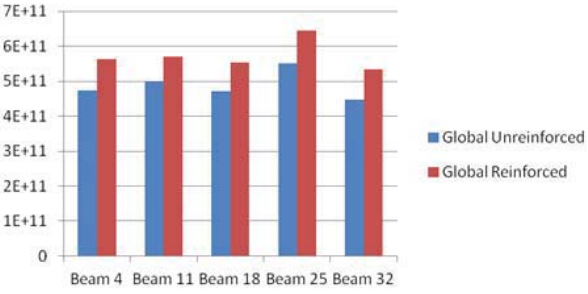

***Figure 14:** Global stiffness data for reinforced (circular grooved) beams (Nmm^2).*

The artificially fractured beams were stiffness tested firstly in their intact unreinforced form and then after the addition of a 3mm saw kerf through the bottom laminate. The results are presented in Figure 15 in relation to local stiffness and in Figure 16 in relation to global stiffness. In their non-fractured, intact state, the beams had a mean global stiffness of $5.23x10^{11}$ Nmm^2 with a standard deviation of $0.397x10^{11}$ Nmm^2 and a mean local stiffness of $5.63X10^{11}$ Nmm^2 with a standard deviation of $0.919x10^{11}$ Nmm^2. After the introduction of the artificial

fracture, the mean global stiffness dropped to 4.53 x10^{11} Nmm^2 with a standard deviation of 0.44x10^{11} Nmm^2 and the mean local stiffness dropped to 3.464 x10^{11} Nmm^2 with a standard deviation of 0.693 x10^{11} Nmm^2. This corresponds to a 13.52% loss in global stiffness with a 6.89% standard deviation and a 38.47% loss in local stiffness with a 15.76% standard deviation.

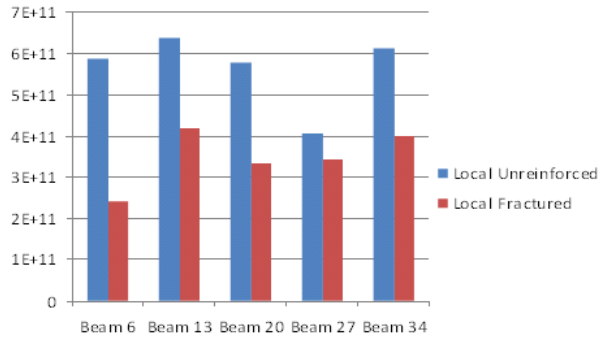

Figure 15: *Local stiffness data for artificially fractured beams (Nmm^2).*

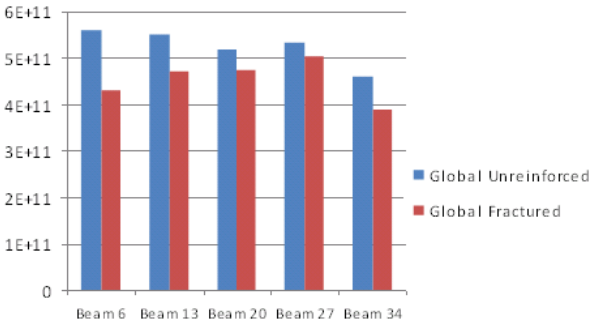

Figure 16: *Global stiffness data for artificially fractured beams (Nmm^2).*

Results from the stiffness testing of the fracture repaired beams are presented in Figure 17 in relation to the local stiffness and in Figure 18 in relation to the global stiffness. In their unreinforced intact state, the beams recorded a mean global stiffness of 5.05 x10^{11} Nmm^2 with a standard deviation of 0.444 x10^{11} Nmm^2 and a mean local stiffness of 5.53 x10^{11} Nmm^2 with a standard deviation of 0.682 x10^{11} Nmm^2. After the fracture and repair procedure for the beams, stiffness testing was undertaken again. The second stiffness test resulted in a mean global stiffness of 5.81 x10^{11} Nmm^2 with a standard deviation of 0.502 x10^{11} Nmm^2 and a mean local stiffness of 6.564 x10^{11} Nmm^2 with a standard deviation of 0.665 x10^{11} Nmm^2. This corresponds to a 15.21% increase in global stiffness with a 3.88% standard deviation and an 18.67% increase in local stiffness with a 4.80% standard deviation.

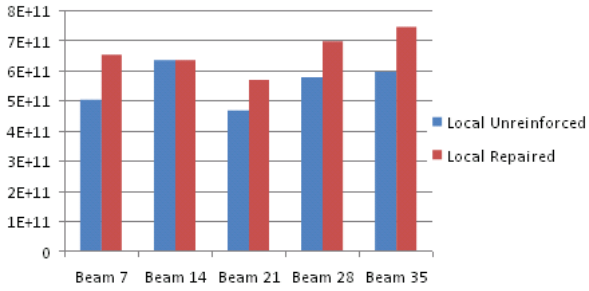

Figure 17: *Local stiffness data for fracture repaired beams (Nmm^2).*

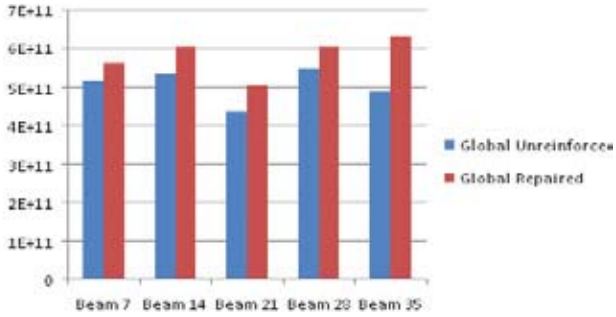

Figure 18: *Global stiffness data for fracture repaired beams (Nmm^2).*

4.1.3 Ultimate Moment Capacity

The ultimate moment capacity M_{ult} achieved by the unreinforced and reinforced beam configurations is given in Table 2. As with the load deflection data, there is a substantial deviation in ultimate moment capacity between the use of bonded in rods being placed in square shaped routed-out grooves and in circular shaped routed-out grooves. The reinforced beams using square shaped grooves achieved an average ultimate moment capacity of 27.35 kNm with the reinforced beams using circular grooves achieving an average of 32.18 kNm. This corresponds to a respective 42.83% and 68.00% increase in ultimate moment capacity compared to the unreinforced controls. The only major difference in the manufacture of these reinforced beams was the shape of the routing head.

The reduction in ultimate moment capacity resulting from a fracture in the bottom tensile lamination is demonstrated in Table 3. For the beams, which were artificially fractured by means of a 3mm saw kerf through the bottom lamination, an average ultimate moment capacity of ultimate moment capacity of 8.81 kNm was achieved. This corresponds to a 54.00% loss in ultimate moment capacity in comparison with the unreinforced control specimens. The potential for use of near surface mounted FRP rods in retrofitting and repair of existing timber structures is demonstrated when beams that are artificially fractured and subsequently repaired achieved an average ultimate moment capacity of 24.69 kNm. This corresponds to a 180% increase in ultimate moment capacity when compared to the fractured beams and a 28.89% increase in ultimate moment capacity when compared to unreinforced control

beams of phase A. Therefore, not only does the use of the technology restore the beams to their initial unreinforced condition but an increase in performance can be achieved.

Table 2: *Ultimate moment capacity for unreinforced and reinforced beams.*

Unreinforced	**M_{ult} (kNm)**	**Reinforced (square grooves)**	**M_{ult} (kNm)**	**Reinforced (circular grooves)**	**M_{ult} (kNm)**
Beam 1	22.94	Beam 3	26.59	Beam 4	34.03
Beam 8	19.78	Beam 10	27.11	Beam 11	32.80
Beam 15	17.45	Beam 17	29.50	Beam 18	34.09
Beam 22	18.58	Beam 24	28.15	Beam 25	31.75
Beam 29	17.01	Beam 31	25.42	Beam 32	28.22
Average (kNm)	19.15	Average (kNm)	27.35	Average (kNm)	32.18
St dev (kNm)	2.38	St dev (kNm)	1.55	St dev (kNm)	2.42
Median (kNm)	18.58	Median (kNm)	27.11	Median (kNm)	32.80
Increase (%)	-	Increase (%)	42.83	Increase (%)	68.00

Table 3: *Ultimate moment capacity for artificially fractured and fracture repaired beams.*

Artificially Fractured	**M_{ult} (kNm)**	**Fracture Repaired**	**M_{ult} (kNm)**
Beam 6	8.15	Beam 7	26.39
Beam 13	6.86	Beam 14	25.11
Beam 20	9.97	Beam 21	27.47
Beam 27	8.41	Beam 28	20.63
Beam 34	10.66	Beam 35	23.83
Average (kNm)	8.81	Average (kNm)	24.69
St dev (kNm)	1.51	St dev (kNm)	2.64
Median (kNm)	8.41	Median (kNm)	25.11
Increase (%)	-	Increase (%)	180.18

4.2 NUMERICAL MODELLING

4.2.1 Load-deflection behaviour

A non-linear finite element model was developed for the unreinforced, reinforced using square shaped grooves and reinforced with circular shaped groove beam configurations with the material properties of specific experimentally tested beams included in the model. The models were incrementally loaded up to the peak load recorded during the testing and the resultant model and experimental load deflection curves were compared in an effort to verify the accuracy of the finite element models, which in turn vindicates the use of the modelling method for further parametric analyses. The comparison of experimental and finite element model data is presented below.

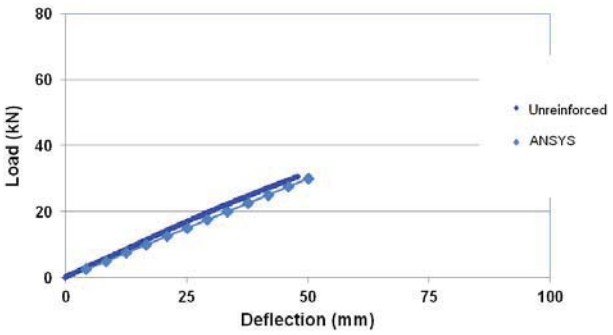

Figure 19: *Predicted versus experimental behaviour for unreinforced beams.*

As illustrated in Figure 19, the load-deflection behaviour predicted by the finite element model is in close agreement with the experimentally determined load-

deflection behaviour. As there is no composite reinforcement material, the loading range is low and behaviour is entirely linear elastic.

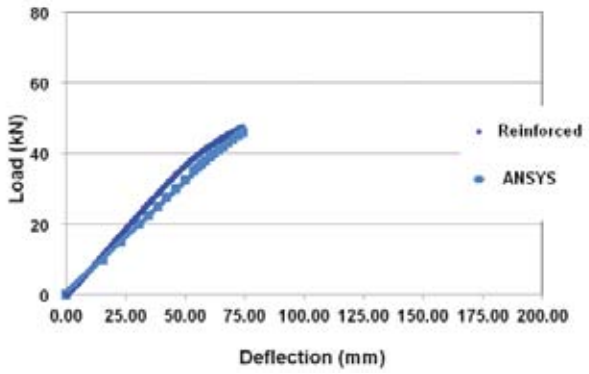

Figure 20: *Predicted versus experimental behaviour for reinforced beams using square grooves.*

The load-deflection behaviour predicted by the finite element model for the reinforced beams which incorporated square grooves shows close agreement with the experimentally determined load-deflection behaviour as illustrated in Figure 20. The non-linear load-deflection behaviour of the experimental beam before failure was also emulated in the finite element model, proving the finite element model to be accurate past the linear elastic range. The stiffness predicted by the FE model is conservative in comparison to the measured stiffness.

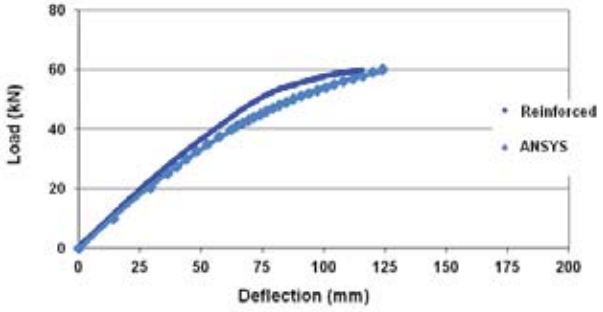

Figure 21: *Predicted versus experimental behaviour for reinforced beams with circular grooves.*

Again, the finite element model shows strong agreement with the experimental load-deflection behaviour of the reinforced beams which included reinforcement in circular grooves (Figure 21). The model is again conservative and emulates the non-linear behaviour of the beam.

4.2.2 Groove analysis

In the experimental testing, it was found that the reinforced beams, which used circular grooves, out-performed the reinforced beams, which used square grooves, in relation to stiffness and ultimate moment capacity. With the finite element model validated against experimental data, the model can be used to examine the stress distribution around these different groove types in an effort to discern whether the experimental performance was due to geometry or whether the difference was as a result of difference in the mechanical properties of the laminations. Two separate models were developed for this analysis, one incorporating the geometry with the square grooves and the other with the geometry of the circular grooves. Apart from the geometry of the grooves, the beams were identical with the same material properties being modelled throughout. The beams were loaded to 40 kN and the stress distribution around each groove was analysed and compared against the alternative orientation. A load of 40 kN was chosen as it was considered large enough to develop substantial stresses throughout the beam. The results from this analysis illustrated that the beams with the circular routed groove enabled a more efficient stress distribution between the reinforcement, the epoxy adhesive and the timber elements. The more efficient stress distribution in turn leads to higher utilisation of the FRP reinforcement. The higher stresses carried by the reinforcement reduce the stresses carried by the timber elements, which results in a beam of higher stiffness and ultimate moment capacity. Therefore, it is adjudged that the superior experimental performance of the reinforced beams that used a circular groove in contrast to a standard square groove was exclusively due to the geometric differences.

5 CONCLUSIONS

The following conclusions were drawn from this study:

- Experimental testing has shown that bonded-in GFRP rods can be used successfully for the flexural repair of fractured glued laminated timber elements.
- The results from the experimental testing suggest that the geometrical arrangement of the routed out grooves is important and enhancements in the mechanical performance of the reinforced and fracture repaired beams can be achieved be reducing the effects of stress concentrations.
- The stiffness of fractured elements can be restored with the use of reasonable reinforcement percentages.
- Significant enhancements in the ultimate moment capacity can be achieved by the repaired beams in comparison to that achieved by fractured and unreinforced beams.
- Ductility is introduced when the GFRP rods are strategically located in the tension zone of the reinforced and repaired glued laminated timber beams.
- The quality of the adhesively bonded interface is of utmost importance in order to preserve the integrity of the repair system.
- A 3-dimensional nonlinear finite element model has been developed, which can predict with reasonable accuracy the stiffness of unreinforced and reinforced beams and the nonlinear behaviour of the reinforced beams. The model agrees with experimental testing that the performance of the reinforced beams can be improved by reducing the stresses by means of the

orientation of the routed-out grooves in which the reinforcement is placed. This is a useful tool which can now be used for further examination of the reinforcement and repair system.

- The long term performance of the GFRP rod repair system in terms of creep and fatigue needs to be investigated.

ACKNOWLEDGEMENT

The financial assistance (University Fellowship) provided by the National University of Ireland, Galway to the primary author is gratefully acknowledged. The authors would like to thank the Department of Civil Engineering, National University of Ireland, Galway for financially assisting the research student, Mr. Conor Whelan. The donation of GFRP materials from Banagher Concrete is most appreciated.

REFERENCES

[1] Hollaway LC, Teng JG. Strengthening and rehabilitation of civil infrastructures using fibre-reinforced polymer (FRP) composites, Woodhead Publishing Ltd. 2008.
[2] Yeomans, D.J., The repair of historic timber structures, Thomas Telford Ltd, 2003.
[3] Ross, P., Appraisal and repair of timber structures, American Society of Civil Engineers (Thomas Telford Ltd.), 2002.
[4] EN 408, Timber structures - structural timber and glued laminated timber – determination of some physical and mechanical properties, 2003.
[5] Raftery G, Harte A, Rodd P. Bonding of FRP materials to wood using thin epoxy gluelines. Int. J. Adhes Adhesv. 29 (5): 580-588, 2009.
[6] Whelan, C. Bonded-in GFRP rods for the repair and strengthening of glued laminated timber beams. MEngSc thesis. National University of Ireland, Galway. 2011.
[7] Bodig, J., Jayne, B.A. Mechanics of wood and wood composites, Krieger publishing company, Malabar, Florida, U.S.A., 1993.
[8] Dinwoodie, J.M. Timber: Its nature and behaviour, 2nd Edition, Taylor and Francis, 2000.
[9] Alam, P. The reinforcement of timber for structural applications and repair, PhD thesis, Dept. of Mechanical Engineering. University of Bath, U.K. 2004.